Lab on a Chip

Micro x-Ray Fluorescence Reveals Pore Space Details and Spatially-resolved Porosity of Rock-based Microfluidic Devices

Journal:	*Lab on a Chip*
Manuscript ID	LC-ART-05-2023-000394.R1
Article Type:	Paper
Date Submitted by the Author:	30-Jul-2023
Complete List of Authors:	Frouté, Laura; Stanford University, Energy Resources Engineering; Guan, Kelly; Stanford University, Energy Resources Engineering Yun, Wenbing; SIGRAY Lewis, Sylvia; SIGRAY Stripe, Benjamin ; Argonne National Laboratory, Center for Nanoscale Materials Yang, Xiaolin; SIGRAY Lapene, Alexandre; TotalEnergies SE Kovscek, A.; Stanford University, Energy Resources Engineering creux, patrice; University of Pau

SCHOLARONE™
Manuscripts

Lab on a Chip

PAPER

Micro x-Ray Fluorescence Reveals Pore Space Details and Spatially-resolved Porosity of Rock-based Microfluidic Devices

Laura Frouté,[a] Kelly Guan,[a] Wenbing Yun,[b] Sylvia JY Lewis,[b] Benjamin D. Stripe,[b] Xiaolin Yang,[b] Alexandre Lapene,[c] Anthony R. Kovscek,[a,e] and Patrice Creux[a,d]

Received 00th May 20xx,
Accepted 00th January 20xx

DOI: 10.1039/x0xx00000x

www.rsc.org/

Characterization of microscopic details of the fabric of mudstones and shales (*i.e.*, structure and composition) is important to understand their storage and transport properties. Current characterization methods struggle to probe reliably multiple scales of interest (*e.g.*, pore and fracture) and measure properties at the finest resolution under representative in-situ conditions. Micro x-ray fluorescence (μXRF) is a high-performance imaging technique that produces elemental images at sub-10 μm spatial resolution and could offer insight into a diversity of shale properties, such as mineral composition, porosity, and in situ pressure gradients. This study designed and carried out a porosity mapping protocol using model and real-rock microfluidic devices and contrast fluids. Etched silicon micromodels with real-rock pore network patterns served as ideal models to establish a proof of concept. Measurements were performed on a novel μXRF microscope not powered by synchrotron radiation. We registered the μXRF datasets with the binary rock masks used for micromodel fabrication and applied segmentation algorithms to compare porosities. We assessed expected advantages and limitations through a sensivity analysis and beam study. μXRF is an important new imaging technique for microfluidic applications.

1. Introduction

Shales and mudstones are defined as laminated fine-grained sedimentary rocks with varying mineral compositions and a wide variety of pore sizes ranging from nanometer pores, conventional pores, to natural fractures[1-2]. Pore networks can be orders of magnitude smaller than conventional systems, leading to 5 to 15% porosities and 0.01 to 10 μD permeabilities[3-5]. Insight into key rock properties, including mineral composition, organic content, porosity, and permeability, is paramount for understanding how shales function as geological seals that prevent upward migration of buoyant fluids, such as carbon dioxide. However, due to their tight pore networks, shales present significant challenges for petrophysical analysis[6-8].

The purpose of this research is to develop a methodology and experimental apparatus capable of probing rock characteristics in-situ with high performance micro x-ray fluorescence (μXRF). μXRF microscopy is an analytical technique that measures the emission of characteristic x-rays from a specimen illuminated by a primary beam of x-rays. By focusing the primary beam to sub-10 μm and rastering it across the surface, the fluorescence emission events collected produce two dimensional (2D) elemental images at 10 μm spatial resolution. Hence, suggesting applicability to dynamic microfluidic processes. Saturating specimens with either a gaseous or liquid contrast agent that emits x-ray fluorescence at high energies can provide elemental maps with a detailed description of rock properties in-situ, pixel by pixel, including porosity, permeability, and an elemental description reflecting mineralogy.

Microfluidics has evolved rapidly to meet the engineering science demands of the flow in geological porous media community including applications combining reaction and transport. For example, devices have been functionalized with calcite[9] or constructed from calcite to study coupled flow and dissolution.[10,11] Monitoring such structural and chemical changes in near real time is challenging; some have proposed confocal Raman microscopy for imaging.[12] Additionally, incorporation of real-rock samples into microfluidics shows great promise to expand understanding of reactive transport and solid-fluid interactions including the evolution of reactive surface area.[13,14]. Natural samples, however, introduce additional chemical complexities that challenge characterization, especially for mudstones.[14]

Given the complexity of shale structures and the novelty of μXRF as a microscopic characterization technique, this study focuses on rock-based micromodels. The objective is to obtain 2D porosity maps of the micromodels and validate the proposed μXRF technique for future use as an imaging tool. To our knowledge this is the first application of an x-ray fluorescence analytical microscope at micron-scale resolution for characterization and monitoring of microfluidic devices.

We begin by reviewing shale characterization techniques and outlining the appeal of μXRF. We discuss the fundamentals of x-ray interaction with matter and present the μXRF prototype along with its intended application. In order to provide a proof of concept for this methodology, we then detail the fabrication of a sandstone

[a] Department of Energy Science and Engineering, Stanford University, Stanford, CA 94305, USA.
[b] SIGRAY, Concord, CA 94520, USA.
[c] Unconventional R&D Program, TOTAL S.A., 64018 Pau, France.
[d] Université de Pau et des Pays de l'Adour, E2S UPPA, CNRS, TotalEnergies, LFCR, 64000 Pau, France
[e] corresponding author, kovscek @stanford.edu

This journal is © The Royal Society of Chemistry 2019

microfluidic rock model, as well as the design of x-ray transparent cells to scan micromodels under static conditions. We present the image acquisition workflow and discuss some of the most relevant results obtained, and their significance for laboratory-scale shale characterization.

2. Shale laboratory-scale characterization: technologies, challenges, scope of improvement

A wide spectrum of laboratory-scale technologies is routinely applied to measure petrophysical attributes of geologic samples from subsurface resources. The most common techniques usually fall into two categories: penetrating fluid type measurements that involve performing mass balances by gravimetry or volumetry (e.g. fluid displacement porosimetry, permeametry, adsorption) and radiation measurements resulting from the excitation of a specimen are collected. The latter include optical, x-ray, electron, neutron or ion spectroscopy and computed tomography[15].

Laboratory penetrating fluid techniques describing pore systems include mercury injection by capillary pressure (MICP), helium (He) pycnometry, gas sorption, and permeability measurements. Sorption isotherms and pore-size distributions are usually determined by low-pressure nitrogen adsorption analysis. Permeability is measured with methods such as step decay and pulse decay[16-20].

While experimental data should theoretically overlap to reveal the full spectrum of structural and behavioural information, depending on the technique, fluid used for measurement, sample preparation, measurement protocol, and data reduction model applied, strong discrepancies can often be observed. For instance, sample preparation has a strong influence on the rock matrix, as cleaning, drying, and crushing can cause alteration and contamination of the pore structure, especially at the sample surface and around its edges[21]. Temperature and control of humidity will determine the state of preservation of fluids, clays and kerogen.

Measurements are also fluid dependent, as pore access is conditioned by kinetic diameter and wettability, and because sorption effects come into play[5,22]. Data analysis models applied to probe pore networks often introduce reductive assumptions of pore geometry and chemical homogeneity, while also neglecting connectivity. As pore sizes and connectivity depend on pore pressure and the effective stress of compaction and cementation (i.e. the difference between overburden and pore pressures), analyses should ideally be performed under proper overburden conditions so as to be representative of reservoir conditions[9]. Porosity and permeability are among the most challenging parameters to be accurately measured due to the difficulty of reproducing in-situ fluid saturations, pore pressure and effective stress conditions[23].

Importantly, one of the sources of disparity involves the very definition of porosity and permeability, with terminologies such as “total”, “effective”, “humid-bound” and “absolute” being used to refer to the pore space measured. All in all, several studies have shown that results obtained from different laboratories can vary significantly[18,24]. Discrepancies in sample handling and measurement conditions easily lead to considerable differences of two to three orders of magnitude[25].

The use of imaging techniques for direct in-situ investigation has become common practice and succeeds in addressing some of these issues. For example, x-ray microscopy and computed tomography (CT) have emerged as powerful tools for multi-scale non-destructive in-situ imaging because they are easy to apply under a variety of experimental conditions and offer fine spatial resolution. X-ray CT has been implemented with sophisticated experimental core holders allowing complex temperature, flow and stress conditions[20-21]. Contrast agents are commonly used to highlight and investigate, quantitatively, the pore network[27-29].

Due to the versatility and performance of the setups and given the considerable penetration depth of high energy x-rays, x-ray CT succeeded in building an in-situ understanding of shale properties. Although useful on centimeter-scale objects, medical CT instruments lack the spatial resolution required for the investigation of pore-scale structures. Similar studies have thus been conducted at higher resolutions on micro (μCT) and nano x-ray systems, bringing an understanding of smaller structural and compositional features[27-32]. While μCT is relatively fast and nondestructive, its resolution is limited to the micron-scale. Nanometer scale resolution is needed to resolve the 3D pore structure that controls the flow and trapping of fluids in shales. Such resolution can only be achieved on a limited number of microscopy and tomography tools.

Scanning electron microscopy (SEM), for example, yields insight into the topography, morphology, and structure of the shale matrix. Focused ion beam (FIB) techniques have been implemented to reconstruct three dimensional (3D) volumes by serial cross-sectioning and imaging[32-35]. High-resolution imaging techniques, however, inevitably limit the field of view studied. Despite nano-scale resolution, extraction of representative networks and upscaling remain colossal tasks.

All in all, the main challenge for quantitative imaging of source rocks is that they are multiscale systems with representative sizes stretching over at least eight orders of magnitude[36]. The validity of pore network considerations derived from imaging techniques is conditioned by the pertinence of the scale chosen. Techniques are invariably subject to a compromise between spatial resolution, field of view, and representativeness of the measurement conditions. Such compromises raise the issue of finding the optimal sample size, resolution, experimental protocol, and image processing method. At this time, multiphysics and multiscale quantitative investigation of shale remains extremely challenging, but it can be achieved using a combination of techniques[37].

Apart from difficulties in capturing the full pore-size range, a considerable shortcoming of the experimental approaches described is their remaining inability to capture transport behavior in-situ. Although steady-state discrete measurements can be performed, and saturation data can be collected during x-ray experiments, techniques often fail to capture flow behavior with elemental contrast, and at temporal and spatial scales of interest. New approaches are needed to study those mechanisms in-situ.

Micromodels (*i.e.*, rock-based platforms that permit visual observation of microfluidic pore-scale phenomena) partially

 This journal is © The Royal Society of Chemistry 2019

succeed in addressing these issues. With their simplified 3D silicon structures mimicking pore networks, they have been used in a wide range of applications (*e.g.*, particle motion, capillary mechanisms and wettability) to complement core-scale rock experiments[38-39]. Nevertheless, they remain 2D-based models that cannot reflect the full structural and mineralogical complexity of shales.

Given these challenges, the main appeal of the µXRF methodology we present lies in its ability to map a variety of properties (including mineralogy, porosity and transport abilities) directly in-situ, with µm-scale resolution. Handheld XRF spectrometers are routine field analytical tools used to recognize diagnostic minerals in outcrops[40]. Advances in x-ray optics have allowed the development of µXRF instruments for chemical characterization and trace elements analysis in geological materials. But µXRF has never been applied, at laboratory-scale, to map in-situ petrophysical properties other than mineralogy, within microfluidic devices[41].

3. µXRF porosity mapping method

3.1. Fundamental Background

As x-ray radiation is focused onto a specimen, interaction with matter mainly results in either the scatter, or the absorption, of the incident x-rays (Fig. 1A). At smaller energies, coherent scattering results from small inhomogeneities in material density or composition. At greater energies, when the incoming photon's energy and path are deviated, the scattering becomes incoherent. An x-ray excitation with an energy higher than an electron binding energy can also knock an electron from the inner shell of an atom. As the incident photon is absorbed, the orbiting electron is either ejected from the atom or promoted to a higher shell. The electron excitation creates a vacancy, causing an electron from a larger energy level to drop down and fill the vacant spot. These vacancies successively de-excite and the excess energy is released, in part, by the emission of secondary x-rays in a process known as fluorescence. Emitted x-ray energies are characteristic of the elements present in the specimen and the energy levels (K and L) of their depleting electron shells.

The proportion of a given interaction event depends on the scanning energy and the nature of the material. Here, we predict x-ray/shale interactions based on the mineralogy of a sample from the Vaca Muerta formation, one of the most prolific shale plays, with estimated technically recoverable resources of 308 TCF gas and 16 Bbbl oil and condensate (Fig. 1B)[44,45]. At energies above 50 keV, x-rays primarily cause scattering. Non-destructive x-ray systems in that energy range measure the attenuation of incident photons and have provided valuable insight into shale's structure, porosity, permeability, mineralogy, thermal and mechanical properties[27,46-47]. At energies below 50 keV, which we will use in this study, x-ray interaction is dominated by absorption, and emitted fluorescence energies reflect the elemental makeup of the specimen.

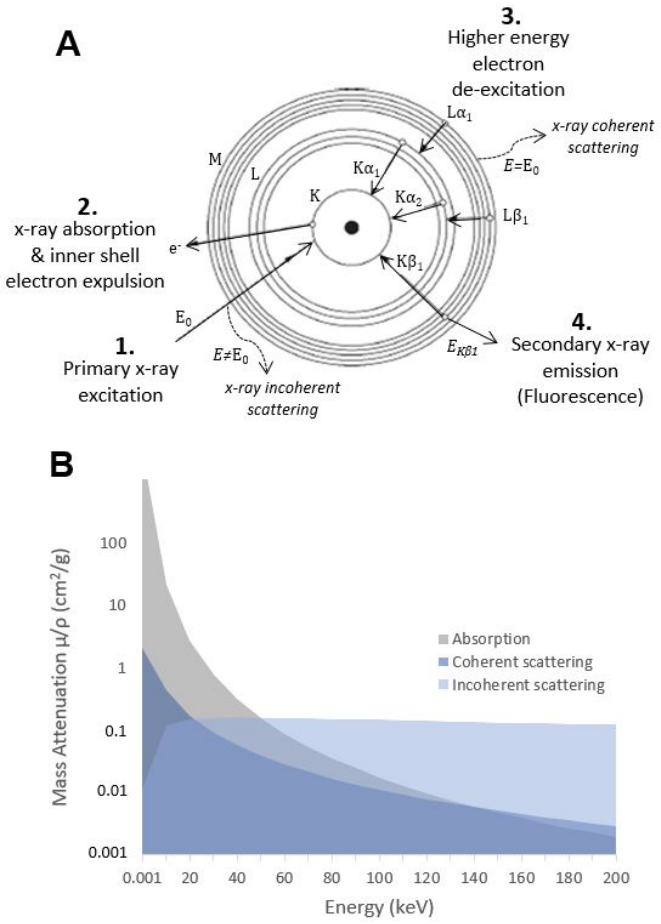

Fig. 1 (A) x-ray interaction diagram (adapted from Cesareo, 2012[42]). (B) Predominance of interaction events for a model Vaca Muerta shale[43]

3.2. X-Ray Equipment & Method

Given the strong x-ray attenuations at low energies, the depth of radiation penetration is a well-known bottleneck for laboratory-scale x-ray fluorescence systems. The Sigray AttoMap™ is a powerful analytical microscope with the highest laboratory x-ray fluorescence detectability, sensitivity and resolution available. Innovations leading to major increases in performance are the system's source and its optics. In conventional laboratory sources, x-ray generation is extremely inefficient, with most of the incoming electron beam energy being dissipated as heat in the target. The intensity of the AttoMap™ source is larger than existing µXRF sources, allowing for better accuracy, sensitivity, and faster scan rates, making in turn the monitoring of fast displacement processes a realistic opportunity. Moreover, the source comprises several x-ray targets (each producing different x-ray spectra) to optimize the sensitivity of specific elements of interest by switching between targets. The optics provide the greatest µXRF spatial resolution available, with beam spot sizes down to 5 µm, for an ideal point source and large working distances of 30 mm. A unique detector with large collection angle captures the photons emitted from the entire beam penetration and x-ray emission path.

A detailed description of a shale specimen's structure and mineralogy, pixel by pixel, can be captured by combining x-ray

fluorescence imaging with the use of a pore contrast fluid within microfluidic setups. Rock sections saturated with a fluorescence marker are exposed to a high-intensity x-ray beam and emit photons along the beam path with distinctive elemental information (Fig. 2A). The recorded fluorescence spectrum displays the signal of all materials in the beam's path, including cell materials, constitutive rock minerals, and the contrast agent. By selecting a specific energy range, and because the detector collects emitted photons in a raster pattern, a 2D elemental map is generated (Fig. 2B).

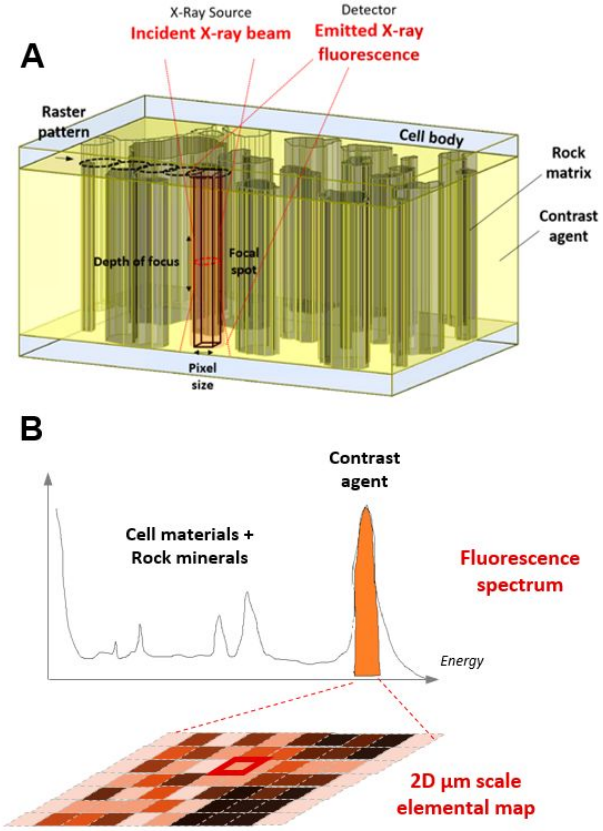

Fig. 2 (A) Capturing x-ray fluorescence emitted by a contrast agent within a microfluidic setup. (B) Selecting a specific x-ray energy range from the collected spectrum to obtain a 2D elemental map reflecting porosity.

Fluorescence signal intensities reflect the total porosity and reveal the rock pore structure, with features that are larger than the system spatial resolution well resolved. Moreover, given the quantitative capabilities of µXRF and its extreme sensitivity, information on connected pores saturated with gas far below the spatial resolution (*e.g.*, 100nm) can be obtained. Under static conditions, fluorescence maps are indicative of the pore volumes filled by the contrast agent. Under dynamic conditions, with known pore volumes, fluorescence can also reflect pressure gradients within the rock matrix. Given the complex 3D structure across shale thin sections, and their small pore volumes, shale imaging might suffer from low x-ray fluorescence counts and will leave the nano-scale pore network spatially unresolved within each pixel. As a result, progressive steps need to be undertaken before scanning rock specimens. In this study, we focus on collecting spatially-resolved descriptions of the porosity of rock-based micromodels in-situ. Two setups of incremental complexity are designed to evaluate the porosity mapping method and its potential for shale characterization. Recorded intensity maps will be compared to the original binary rock pattern to verify that they accurately reflect the fluid content in the targeted regions.

3.3. Experimental setups

Rock-based micromodels. Micromodel fabrication follows a well-established UV nanolithography protocol involving silicon wafer drying, photoresist spin coating, mask alignment, UV exposure, development, etching, drilling of injection ports, and removal of resin[37-39]. The mask design is comprised of injection ports, flow channels and a central 5 x 5 cm rock matrix array featuring a periodic arrangement of 23 x 8 porous sandstone base patterns, Fig. 3. Note the scale bar in Fig. 3B. Pore throat dimensions are on the order of 10's µm whereas body sizes are 100's µm. Image analysis computes an overall porosity value of 54%. Topographic measurements of the final wafers are acquired with an optical profiler, revealing uniform etching depths. An optically flat borosilicate glass cover is anodically bonded to the surface of the etched silicon wafer. Once sealed inside a microfluidic holder, the 3D pattern is filled with a contrast agent at low injection pressures to highlight the pore network.

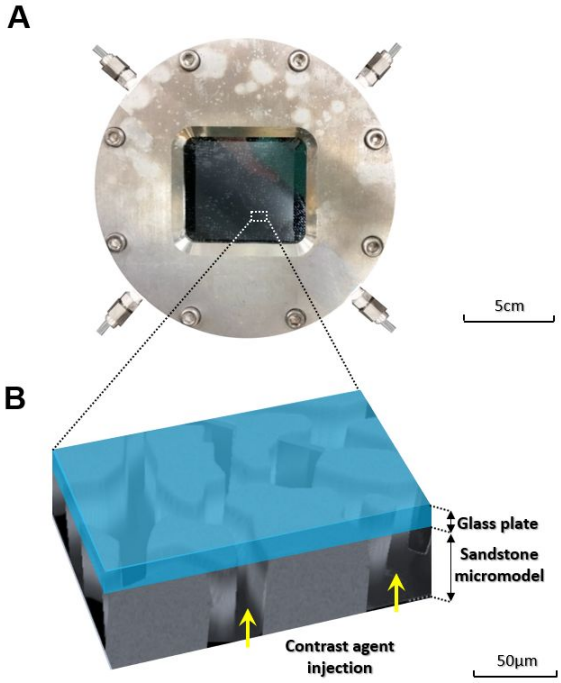

Fig. 3 (A) Micromodel holder. (B) Detail of the micromodel structure.

Rubidium fluorescence maps are expected to provide a recognizable description of the sandstone pattern because the contrast solution is confined to the sandstone pattern, with grain dimensions larger than the microscope spatial resolution and minimal x-ray attenuation through the glass plate. Acquired images can then be registered with the original binary pattern.

This journal is © The Royal Society of Chemistry 2019

Please do not adjust margins

Selection, concentration, and distribution of the contrast agent are critical to yield quantitative porosity measurements. In order to minimize x-ray attenuation, we chose a 175 µm thick glass cover that permitted good X-ray penetration, but it considerably limited possible injection pressures. In order to achieve high molecular concentrations at low pressures and avoid leaks, contrast solutions are used rather than gases on this setup. A 35 wt% aqueous solution is prepared with high-energy rubidium chloride (RbCl) salts. Rubidium (Rb) has fluorescence emission energies of $K_{\alpha1,Rb}$ = 13.39 keV and $L_{\alpha1,Rb}$ = 1.69 keV.

Polycarbonate cell. The purpose of this second static setup, once validated, is to later accommodate shale thin sections. The cell is comprised of two parts that mate together and are sealed using screws (Fig. 4C). Once enclosed, the 600 µm-high cavity can be vacuumed, saturated with a contrast gas and imaged through the top window. Krypton (Kr), a common contrast agent in x-ray systems, is chosen for its emission energy of 12 keV. In order to minimize x-ray attenuation, the cell is manufactured from polycarbonate sheets. The inlet and outlet are connected to a small setup for gas supply and pressure monitoring. The design is capable of withstanding pressures up to 5 bar. In this study, the cell holds unbonded micromodel pieces placed at the bottom of the cavity. The major difference compared to the previous setup is that the pore networks are not confined, and both the gas within the pores and in the cavity above contribute to the fluorescence counts collected.

Because the cell is meant to host rock sections in the future and the presence of gas above the sample might impair detectability, we perform two types of experiments. The first involves sandstone micromodel pieces for pore volume measurement (Fig. 4A). A sensitivity study on pore detectability is also conducted with varying pore sizes (0.1 - 90 µm) and varying gas pressures (2.5 - 5 bar). For that purpose, a 5-pores micromodel block is manufactured using nanolithography (25 - 90 µm pores), as well as FIB-SEM milling (0.1 - 1 µm pores) (Fig. 4B).

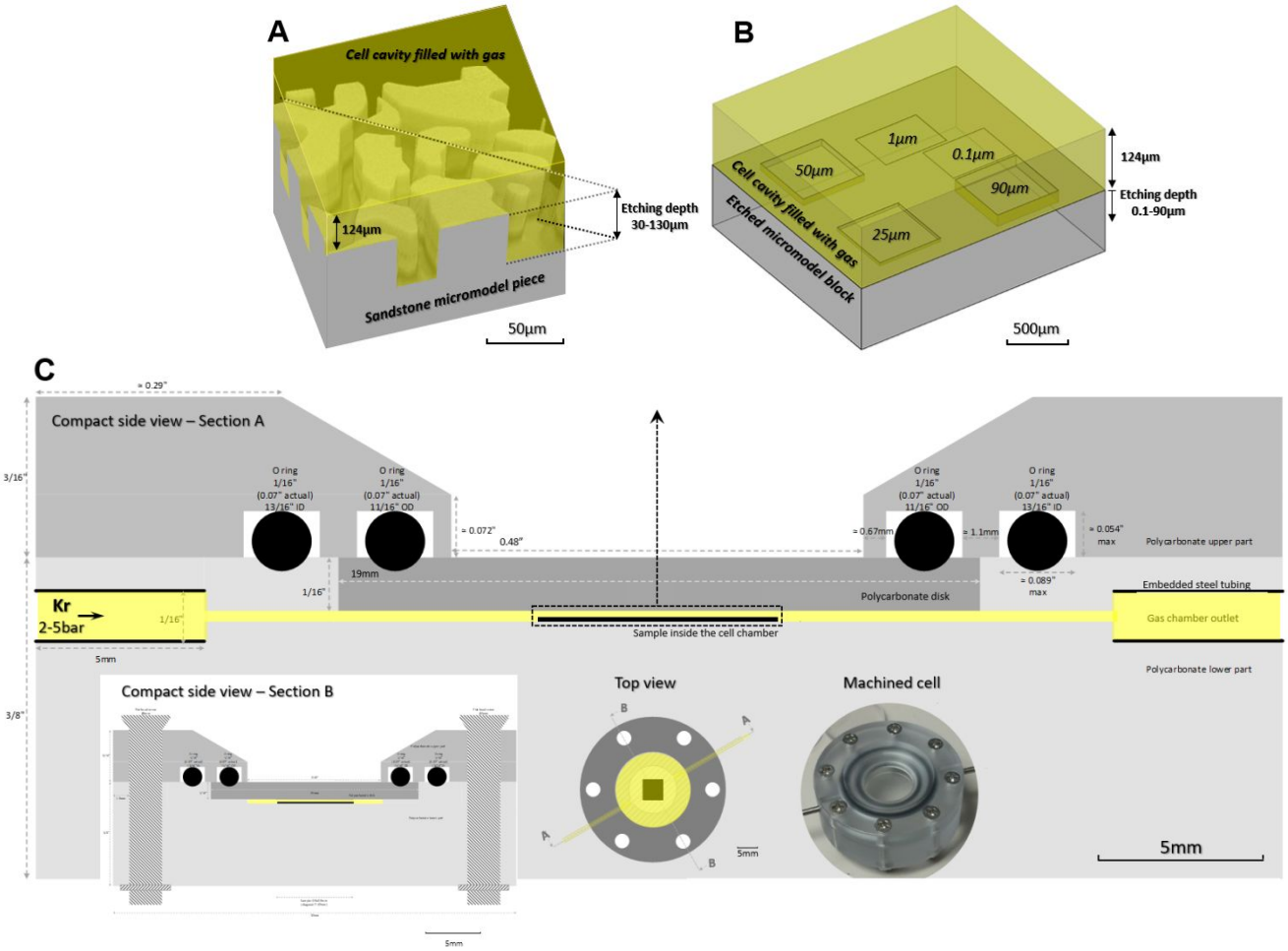

Fig. 4 (A) Detail of the sandstone micromodel piece inside the cell chamber. (B) Detail of the 5-pores micromodel chip inside the cell chamber. (C) 2D schematic overview of the static polycarbonate cell, with a picture of the machined product.

4. Results and discussion

Acquisition of µXRF maps. The experimental cells are set on the microscope stage, under the source and as close as possible to the detector. The imaging protocol consists of a few acquisitions at low resolution, in order to identify and focus on recognizable features such as the edges of the cell, one of the injection ports, or the edge of the micromodel pieces. Then, images are collected at progressively increasing magnification to image regions of interest.

We perform a series of scans both in the micromodel holder, and inside the polycarbonate cell.

Table 1 summarizes the settings for some of the most significant scans. Scans 1 through 3 are carried out with the RbCl solution in order to perform porosity calculations and pattern registration. Beam profiles and spatial resolutions are improved between scans. Scan 4 is performed on micromodel pieces with varying etching depths inside the polycarbonate cell filled with Kr in order to validate that elemental counts reflect pore volumes, despite having no confinement of the pore structures. Scan 5 assesses x-ray fluorescence sensitivity to pore size and pressure using the micromodel chip.

Table 1 Summary of scan settings.

Measurement settings	SCAN 1	SCAN 2	SCAN 3	SCAN 4	SCAN 5
Source voltage (kV), current (mA), power (W)	35, 0.2, 7	35, 0.2, 7	35, 0.2, 7	50, 0.2, 10	30, 0.66, 20
Pixel size (µm)	10.25	10	5	10	40
Image size (µm)	3700x3099	3000x3000	500x500	2500x2500	1480x1560
Acquisition time (h)	21.2	12.6	1.4	15	1.6
Contrast agent ($E_{emission\ Ka}$, keV)	RbCl 35wt% (13.4)	RbCl 35wt% (13.4)	RbCl 35wt% (13.4)	Kr, 4.5bar (12.6)	Kr, 2.5 and 5bar (12.6)
Etching depth (µm)	30	30	30	30 and 130	0.1 to 90
Cell	Micromodel holder	Micromodel holder	Micromodel holder	Polycarbonate cell	Polycarbonate cell
Porous system	Rock-based micromodel	Rock-based micromodel	Rock-based micromodel	Rock-based micromodel	Micromodel chip
	Rubidium: porosity calculations in confined sandstone-based micromodels			Krypton: multi-system, multi-depth tests in polycarbonate cell	

For all scans, the energy spectra display an elastic continuum background and scattered peaks from the primary beam, as well as element-specific fluorescence emission peaks. The high signal-to-noise ratios (SNR) measured for the contrast agents allow the production of elemental maps with good resolution and contrast (Fig. 5). For images where the sandstone pattern is recognizable, we perform a semi-automated 2D registration. The raw acquired image is first manually rotated, cropped and resized. 2D registration functions in MATLAB are then used to find and perform the geometric transformations that align the µXRF image with the binary mask. Image blurriness is corrected by applying a Poisson denoising algorithm (Richardson-Lucy deconvolution)[42]. For maps where the pore networks are resolved, the images are thresholded with Otsu's method to produce high-quality, binary images[43].

Porosity segmentation. The rubidium maps acquired with confined sandstone-based micromodels in scans 1 through 3 are shown in Fig. 5. The smallest grain dimension (about 10 µm) is comparable in size to the µXRF spatial resolution (a few micrometers), and because the porous network is confined, the sandstone pattern is recognizable. Elemental images are registered with the binary mask used for micromodel fabrication, with only minor misalignments (Fig. 5). The rubidium fluorescence histogram is a clean bimodal distribution. By displaying the spatial distribution of intensity increments, we observe that the rubidium composition is uniform within the micromodel. Therefore, the fluorescence distributions are solely indicative of structural features. This verification is crucial for experiments with the rubidium solution, whose concentration needs to remain uniform during the acquisition.

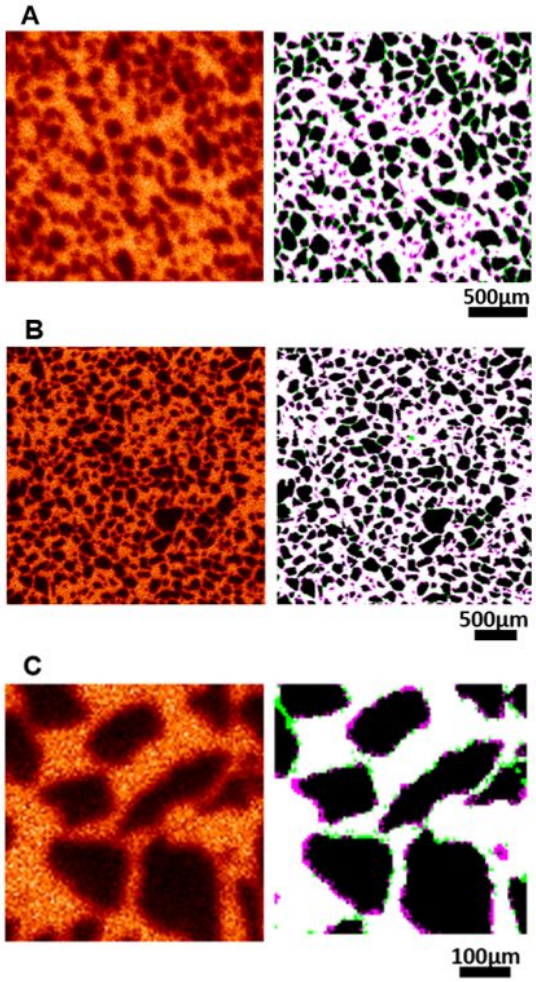

Fig. 5 Rubidium fluorescence maps and misalignment after registration with the binary mask (black: overlapping grain patterns, pink: grain patterns absent in the mask; green: grain patterns absent in the raw µXRF image). (A) Scan 1. (B) Scan 2. (C) Scan 3.

This journal is © The Royal Society of Chemistry 2019

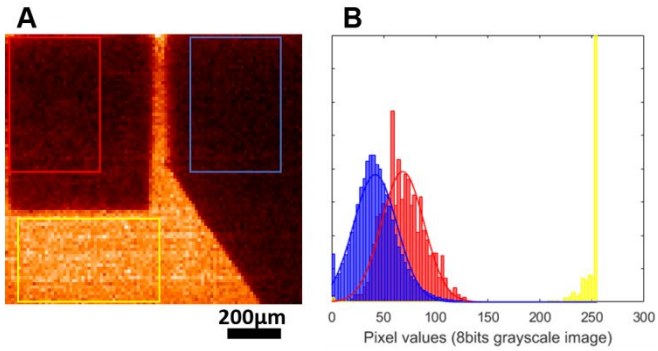

Fig. 6 (A) Krypton fluorescence map obtained with the polycarbonate cell containing micromodel pieces (Scan 5). Regions of interest overlay the shallow micromodel (blue), the deep micromodel (red), and the cell chamber (yellow). (B) Associated histograms with Gaussian fitting reflect the differences in Kr volumes.

Table 2 Results of porosity segmentation.

Scan 1	**53.82**	53.13
Scan 2	**52.7**	51.7
Scan 3	**48.2**	49.41

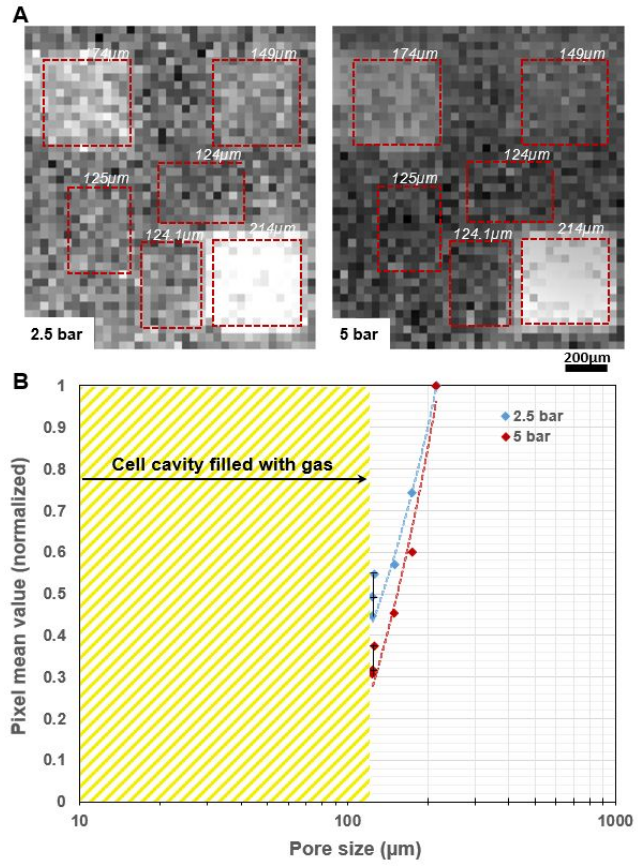

Fig. 7 (A) Maps acquired of the 5-pores micromodel block at 2.5 and 5 bars krypton pressure. (B) Sensitivity of the method to pore sizes and pressures.

We also assume that the dimensions of the micromodel features match those of the binary mask, and that grain edges are perfectly vertical. This is corroborated by optical profiling performed on some of the silicon wafers. Thus, grains and voids contribute equally to edge blurriness for pixels where an overlap occurs, and the porosity of the 3D micromodel matches that of the 2D mask binary mask. All in all, the grayscale palette used to quantify rubidium fluorescence counts is directly proportional to the volume ratio filled by the contrast solution, which in turn directly reflects the porosity of the binary mask used for micromodel fabrication. Because it is consistent with the geometry of the system, we begin by estimating porosity through an arithmetic mean over the normalized dataset. For scan 2 (Fig. 5B), we compute a value of 48.1%, which is close to the known mask porosity of 52.7%. This simple method, which relies strictly on fluorescence intensity statistics in the rubidium energy range without any image processing, is therefore remarkably accurate. Spectral deconvolution followed by segmentation via thresholding greatly reduce the uncertainty. Segmentation yields the porosity values given in Table 2. In all experimental cases (Fig. 5), we find that the calculated porosities agree with known pore volumes within 1% (Table 2).

Towards rock experiments. Scans are also performed on unconfined sandstone micromodel pieces in the static polycarbonate cell with krypton. Fig. 6 shows an example, where two pieces of micromodel of different etching depths are placed in the chamber and pressurized. The rock pattern is no longer spatially resolved. We select 3 areas of equal dimensions overlaying the shallow micromodel, the deep micromodel, and the empty cell chamber. Gaussian probability functions are fitted to the fluorescence distributions to compute experimental krypton pore volume ratios. Known pore volume ratios are estimated based on depth differences and an average micromodel porosity of 54%. The results, presented in Table 3, show that the elemental counts in both micromodels reflect the pore volume differences within 2%. This speaks to the sensitivity of the method and its ability to reflect 2D structural properties, even sub-resolution, when grain patterns are no longer recognizable.

Table 3 Results of pore volume calculations (Scan 5).

Region	Available depth (µm)	Known Kr pore volume ratios (%)	Measured Kr pore volume ratios (%)
Shallow micromodel	117	**16.5**	16.4
Deep micromodel	217	**25.1**	26.7
Chamber	626	**100**	100

In order to study sub-resolution detectability, a sensitivity study is conducted with varying pore sizes (0.1 - 90 µm) and two gas pressures (2.5 - 5 bar). Fig. 7A shows the fluorescence maps acquired, with indications of the pore locations and total krypton depths. Fig. 7B compares the normalized mean fluorescence measured for each pore to the known pore sizes. We observe that, for both pressures, similar linear trends are obtained, showing that elemental counts closely reflect depth differences. We note that because the pore models were

unconfined, with a Kr overhead cap of 124 µm, the pore size interval studied was limited between 124 and 214 µm. The measurements show that pore dimensions down to 1 - 2% of the maximum pore size can be quantified accurately. The detectability of 0.1 µm and 1 µm increments (respectively 0.08% and 0.8% in height variability) then becomes difficult to measure, although close to the expected range nonetheless. Finally, we also note that increasing the pressure improves accuracy and reduces standard error. These results suggest that, with a thinner gas cap and a higher pressure, pore sizes well below 1% of the largest pore dimension could be detected. The large sensitivity range and sub-resolution detectability make the AttoMap™ a relevant opportunity for the imaging of real rock properties.

The current depth of field of the microscope is approximately 200 µm (100 µm on both sides of the optimum plane of focus). Within that range, a thin section of rock would be in focus and the spot size can be considered the same as the focal spot size. Outside of that range, the beam has an hourglass shape, with the spot size increasing with the distance from the convergence plane (Fig. 2A). Outside of the depth of field, atoms receive a more spread-out beam, so the interaction surface is larger, but the photon flux itself is slimmer. For instance, a 500 µm thin section of rock with a focal spot size of 10 µm at mid-height would have a spot size of about 15 µm at its surface. On the Sigray AttoMap™, the un-collimated fluorescence signal is collected from the entire beam penetration and photon emission path; therefore, if the sample is thicker than the depth of field, the photon flux received per cross-section varies along the material depth. Consequently, for a thick and complex shale thin section, matrix absorption and uneven excitation along the beam path without confocal vertical resolution can be problematic for interpretation of the fluorescence intensity maps. On the other hand, the larger the sample, the more abundant the fluorescent pores on the beam path and the more structural information there is to be extracted. As a result, the thickness of the rock should ideally match the depth of field of 200 µm. Thicker specimens, although easier to prepare and more statistically representative of the material properties, will be examined will smaller accuracy. To maximize the photon flux (SNR) for a broad range of elements, the Sigray AttoMap™ beam originating from the tungsten target has no monochromator (*i.e.*, the sample is illuminated by the full tungsten spectrum instead of narrowing the incoming beam down to a single energy range). As attenuation is energy dependent, there are minor vertical disparities in the beam profile exciting the sample, leading to a greater background in the energy spectrum. Due to anticipated issues stemming from small shale specimen thickness, small pore sizes, mineral heterogeneities, and x-ray self-attenuation, additional tests are necessary to ensure sufficient detectability within thin sections.

Application to rock samples. To test our methodology on real rocks, we chose two samples: a carbonate and a shale. The carbonate is a Texas Cordova Cream (Kocurek Industries, Caldwell, TX). The porosity measured is 24.6% using mercury intrusion pressure and He pycnometry. The result is comparable to reported literature values of 24 - 25% from core plug measurements[50]. The shale sample is from the Vaca Muerta formation in Argentina (TotalEnergies, Pau, France). Its porosity was measured as 4.5% using He pycnometry. Krypton gas was used here to invade fully the connected pore space of the two samples and provide a contrast agent for imaging.

Various zones were scanned including shale matrix, Texas Cream matrix, and bulk phase. First, the two points: 0% (noise and impurities) and 100% bulk impurities are represented. The normalized k_α counts average values for the shale sample and Texas Cream. The corresponding porosity is deduced via the straight line between the two extremes points and the slope of the line is 0.99. This result confirms the excellent linearity of the detector included for very low signals. Deduced porosities are 25% for Texas Cream and 5 % for the shale sample in agreement with prior measurement.

Future Development. This study has pioneered microXRF for microfluidics under static conditions where pressure is constant. Fluorescence signal intensities are proportional to gas pressure. Hence, under dynamic conditions, with characterized porosity, fluorescence intensity reflects pressure gradients and the pathways carrying the greatest flow within the rock matrix. Characterization of steady-state and transient flow is an area of future work that will be enabled by further development of nonsynchrotron microXRF systems and reduction in image acquisition time. Additionally, we intend to demonstrate mineralogy mapping including cation exchange within clay minerals.

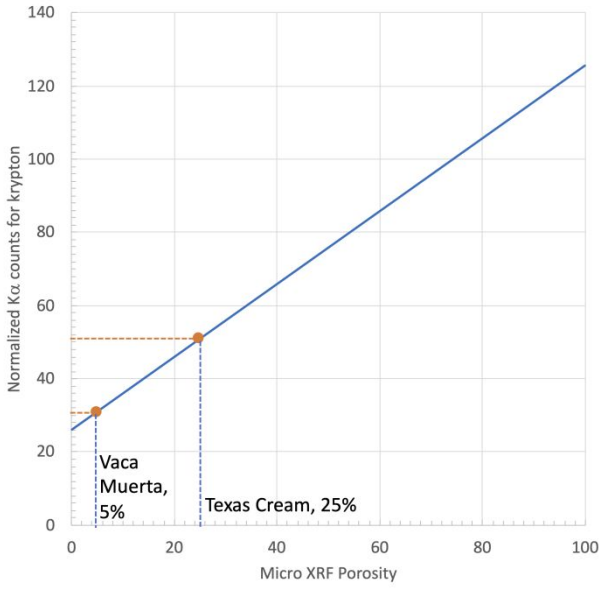

Fig. 8: Porosity measurement of Vaca Muerta Shale and Texas Cream carbonate samples via micro XRF exploiting the linearity of the detector.

5. Conclusion

We report the development of an imaging methodology and the fabrication of microfluidic devices to investigate porous media under in-situ conditions. We describe an innovative technique

This journal is © The Royal Society of Chemistry 2019

to map porosity within rock samples by micro x-ray fluorescence and obtain a proof of concept on ideal micromodel geometries. The μXRF imaging platform provides energy spectra reflecting the spatially resolved relative presence of elements. We find that the instrument succeeds in producing quantitative pore volume maps of model porous media saturated with a contrast agent. We visualize bimodal structures, perform registration to align the fluorescence datasets with the binary masks, and apply segmentation algorithms to calculate porosities with excellent accuracy (within 1 - 2%).

The μXRF microscope, however, has much greater potential than demonstrated with simplified rock-based models. A study of micromodel pieces in the static polycarbonate cell shows that pore volume measurements can be carried out very accurately, even with no insight into the pore structure. The large sensitivity range and sub-resolution detectability provide a realistic opportunity for the characterization of shale specimens, whose pore dimensions and properties notoriously extend to the nanoscale. In the longer term, we expect that a cell with lateral rock confinement will allow for dynamic monitoring and visualization of gas-pressure gradients through a rock sample to estimate absolute permeability.

One limitation revealed by considerations of x-ray excitation volumes is the narrow vertical field of view. Although elemental maps acquired can be at centimetre-scale, sample thickness should not exceed a few hundred micrometres. Additional improvements in the AttoMap™ capabilities and the microfluidic design will further increase beam intensities, improve detectability, broaden the vertical field of view, and unlock advanced capabilities for the quantification of petrophysical properties. Drawing from our demonstrations on rock-based micromodels, the high sensitivity, astigmatism, large detectability range and fine spatial resolution of this laboratory-scale technique have the potential to provide valuable physical insights regarding porous media. We find capability to characterize systems with large pores (> 5 μm) and to obtain a chemical composition mapping of the 3D porous media. Due to the large sensitivity of microXRF, it is also accurate to measure the porosity of very complex rocks based on a quantification of X-ray fluorescent molecules to access details of the tightest pores and their contribution to the volume. The efficiency is quite similar to He pycnometry and also informs about heterogeneities and mineral structures.

Conflicts of interest

There are no conflicts to declare.

Acknowledgements

The authors gratefully acknowledge TOTAL S.A. for its support through the STEMS project, a research collaboration between TOTAL S.A. and Stanford University. Micro-machining and lithography were performed in the SNF and SNSF labs at Stanford that are supported by the National Science Foundation as part of the National Nanotechnology Coordinated Infrastructure under award ECCS-1542152. The authors also acknowledge Cynthia M. Ross, Sophie Roman, and Tim Anderson from the Department of Energy Resources Engineering at Stanford, for their expertise in microfluidics and image processing.

References

1 M. Mehana and I. El-monier, *Petroleum*, 2016, **2**, 138-147.
2 R.G. Loucks, R.M. Reed, S.C. Ruppel and D.M. Jarvie, *Journal of Sedimentary Research*, 2009, **79**, 848-861.
3 P.H. Nelson, *AAPG Bulletin*, 2009, **93**, 329-340.
4 M. Fleury and M. Romero-Sarmiento, *J. Petroleum Science and Engineering*, 2016, **137**, 55-62.
5 S. Saraji, M. Piri, *International Journal of Coal Geology*, 2015, **146**, 42-54.
6 P. Zhang, L. Hu, J.N. Meegoda and S. Gao, *Sci. Rep.*, 2015, **5:13501**.
7 F. Javadpour, D. Fisher and M. Unsworth, *J. Can. Petrol. Technol.*, 2007, **46**, 55–61.
8 A. Beskok and G.E. Karniadakis, *Microscale Thermophys. Eng.,* 1999, **3**, 43–77.
9 Song, W, F Ogunbanwo, M Steinsbø, M A. Fernø, and A R. Kovscek,*Lab on a Chip* **18**, no. 24 (2018): 3881-3891.
10 Song, W, T W. de Haas, H Fadaei, and D Sinton, *Lab on a Chip* **14**, no. 22 (2014): 4382-4390.
11 Soulaine, C, S Roman, A R Kovscek, and i A. Tchelepi, *Journal of Fluid Mechanics* **827** (2017): 457-483.
12 Poonoosamy, J, C Soulaine, A Burmeister, G Deissmann, D Bosbach, and S Roman. *Lab on a Chip* **20**, no. 14 (2020): 2562-2571.
13 Deng, H, J P. Fitts, R V Tappero, J J Kim, and C A Peters, *Environmental Science & Technology* **54**, no. 19 (2020): 12502-12510.
14 Ling, Bo, M Sodwatana, A Kohli, C M Ross, A Jew, A R Kovscek, and I Battiato, *Proceedings of the National Academy of Sciences* **119,** no. 32 (2022): e2122520119.
15 R. M. Bustin, A. Bustin, D. Ross, G. Chalmers, V. Murthy, C. Laxmi, and X. Cui, presented at the AAPG Annual Convention, San Antonio, April 20-23, 2008.
16 H. Darabi, A. Ettehad, F. Javadpour and K. Sepehrnoori, *J. Fluid Mech.,* 2012, **710**, 641–658.
17 H. Jang, J. Lee and W. Lee, *Environ. Earth Sci.,* 2015, **74**, 3333–3343.
18 S. Profice, G. Hamon and B. Nicot, paper SCA 2015-021 presented at the International Symposium SCA, St. John's, August 16-21, 2015.
19 Y. Dadmohammadi, S. Misra, C. Sondergeld, C. Rai, *J. Pet. Sci. Eng.,* 2017, **158**, 554–569.
20 P. Suri, M. Azeemuddin, M. Zaman, A.R. Kukreti, J.C. Roegiers, *J. Pet. Sci. Eng.* 1997, **17**, 247–264.
21 American Petroleum Institute, *Recommended Practices for Core Analysis*, API, Washington, 1998.
22 J.C. Glorioso and A. Rattia, paper SPE-153004 presented at the SPE/EAGE European Unconventional Resources Conference and Exhibition, Vienna, March 20-22, 2012.
23 X. Cui, A.M.M. Bustin and R.M. Bustin, *Geofluids*, 2009, **9**, 208-223.
24 Q.R. Passey, K.M. Bohacs, W.L. Esch, R. Klimentidis and S. Sinha, paper SPE-131350 presented at the CPS/SPE International Oil & Gas Conference and Exhibition, Beijing, June 8-10, 2010.

25 C.H. Sondergeld, K.E. Newsham, J.T. Comisky, M.C. Rice and C.S. Rai, paper SPE-131768 presented at the SPE Unconventional Gas Conference, Pittsburgh, February 23-25, 2010.
26 M. Voltolini, H. Barnard, P. Creux and J. Ajo-Franklin, *J. Synchrotron Rad.,* 2019, **26**, 238-243.
27 G. Glatz, L.M. Castanier and A.R. Kovscek, *Energy Fuels*, 2016, **30**, 8141-8149.
28 B. Vega, A. Dutta and A.R. Kovscek, *Transp Porous Med*, 2014, **101**, 81-97.
29 C.H. Arns, F. Bauget, A. Limaye, A. Sakellariou, T.J. Senden, A.P. Sheppard, R.M. Sok, W.V. Pinczewski, S. Bakke, L.I. Berge, P.E Øren, paper SPE-90368 presented at the SPE Annual Technical Conference and Exhibition, Houston, September 26-29, 2004.
30 C. Soulaine, F. Gjetvaj, C. Garing, S. Roman, A. Russian, P. Gouze and H.A. Tchelepi, *Transp Porous Med*, 2016, **113**, 227-243.
31 L. Tomutsa, D.B. Silin and V. Radmilovic*, SPE Reservoir Evaluation & Engineering*, 2007, **10**, 285-293.
32 R. Wirth, *Chem. Geol.,* 2009, **261**, 217–229.
33 G.R. Chalmers, R.M. Bustin and I.M. Power, *AAPG Bulletin*, 2012, **96**, 1099-1119.
34 M.E. Curtis, C.H. Sondergeld, R.J. Ambrose and C.S. Rai, *AAPG Bulletin*, 2012, **96**, 665-677.
35 S. Zhou, G. Yan, H. Xue, W. Guo, X. Li, X., *Marine and Petroleum Geology*, 2016, **73**, 174-180.
36 A. Steinbach, H. Bale, M. Andrews and S. Bhattiprolu, presented at the Workshop on Digital Rock Physics Derived Rock Mechanics Properties, San Francisco, June 2015.
37 A. Busch, K. Schweinar, N. Kampman, A.B. Coorn, V. Pipich, A. Feoktystov, L. Leu, A. Amann-Hildenbrand and P. Bertier, *Geological Society of London*, 2017, **454**.
38 M. Buchgraber, M. Al-Dossary, C.M. Ross and A.R. Kovscek, *Journal of Petroleum Science and Engineering*, 2012, **86-87**, 27-38.
39 M. Buchgraber, T. Clemens, L.M. Castanier and A.R. Kovscek, *SPE Reservoir Evaluation & Engineering*, 2011, **14**, 269-280.
40 K.E. Young, C.A. Evans, K.V. Hodges, J.E. Bleacher and T.G. Graff, *Applied Geochemistry*, 2016, **72**, 77-87.
41 S. Flude, M. Haschke and M. Storey, *Mineralogical Magazine*, 2017, **81**, 923-948.
42 R. Cesareo, in *Ullmann's Encyclopedia of Industrial Chemistry*, Wiley, Weinheim, 2012, X-Ray Fluorescence Spectrometry, 595-629.
43 X-Ray Form Factor, Attenuation, and Scattering Tables (NIST), https://physics.nist.gov/PhysRefData/FFast/html/form.html (accessed July 2016)
44 U.S. Department of Energy, *Technically Recoverable Shale Oil and Shale Gas Resources: Argentina*, EIA, Washington, 2015.
45 F. Herrero, L. Maschio and S. Maria, paper URTeC 1965548 presented at the Unconventional Resources Technology Conference, Denver, August 25-27, 2014.
46 F. Mees, R. Swennen, M. Van Geet and P. Jacobs, *Applications of X-ray computed tomography in the geosciences*, Geological Society, London, 2003.
47 T.M. Buzug, *Computed Tomography: From Photon Statistics to Modern Cone-Beam CT*, Springer, Berlin-Heidelberg, 2008.
48 M.K. Khan, S. Morigi, L. Reichel and F. Sgallari, Numer. *Math. Theor. Meth. Appl.*, 2013, **6**, 1-15.
49 N. Otsu, *IEEE Transactions on Systems, Man, and Cybernetics*, 1979, **9**, 62-66.
50 A. Alshehri and A.R. Kovscek, SPE Journal, 2016, **21**(05), 1631-1342.

 This journal is © The Royal Society of Chemistry 2019